

## Spectroscopic Constraints on the Build-up of the Intracluster Light in the Coma Cluster

MENG GU,<sup>1</sup> CHARLIE CONROY,<sup>1</sup> DAVID LAW,<sup>2</sup> PIETER VAN DOKKUM,<sup>3</sup> RENBIN YAN,<sup>4</sup> DAVID WAKE,<sup>5</sup> KEVIN BUNDY,<sup>6</sup>  
ALEXA VILLAUME,<sup>6</sup> ROBERTO ABRAHAM,<sup>7</sup> ALLISON MERRITT,<sup>8</sup> JIELAI ZHANG,<sup>9</sup> MATTHEW BERSHADY,<sup>10,11</sup>  
DMITRY BIZYAEV,<sup>12,13</sup> KAIKE PAN,<sup>12</sup> DANIEL THOMAS,<sup>14</sup> AND ANNE-MARIE WEIJMANS<sup>15</sup>

<sup>1</sup>*Department of Astronomy, Harvard University, Cambridge, MA 02138, USA*

<sup>2</sup>*Space Telescope Science Institute, 3700 San Martin Drive, Baltimore, MD 21218, USA*

<sup>3</sup>*Astronomy Department, Yale University, New Haven, CT 06511, USA*

<sup>4</sup>*Department of Physics and Astronomy, University of Kentucky, 505 Rose Street, Lexington, KY 40506-0057, USA*

<sup>5</sup>*Department of Physical Sciences, The Open University, Milton Keynes, MK7 6AA, UK*

<sup>6</sup>*Department of Astronomy and Astrophysics, University of California, Santa Cruz, CA 95064, USA*

<sup>7</sup>*Department of Astronomy and Astrophysics, University of Toronto, 50 St. George Street, Toronto, ON M5S 3H4, Canada*

<sup>8</sup>*Max-Planck-Institut für Astronomie, Königstuhl 17, D-69117 Heidelberg, Germany*

<sup>9</sup>*Schmidt Science Fellows, in Partnership with the Rhodes Trust, Rhodes House, Oxford, OX1 3RG, UK*

<sup>10</sup>*Department of Astronomy, University of Wisconsin-Madison, 475N. Charter Street, Madison WI 53703, USA*

<sup>11</sup>*South African Astronomical Observatory, P.O. Box 9, Observatory 7935, Cape Town, South Africa*

<sup>12</sup>*Apache Point Observatory, P.O. Box 59, Sunspot, NM 88349, USA*

<sup>13</sup>*Sternberg Astronomical Institute, Moscow State University, Moscow, Russia*

<sup>14</sup>*Institute of Cosmology & Gravitation, University of Portsmouth, Dennis Sciama Building, Portsmouth, PO1 3FX, UK*

<sup>15</sup>*School of Physics and Astronomy, University of St. Andrews, North Haugh, St. Andrews KY16 9SS, UK*

### ABSTRACT

The stellar content of the intracluster light (ICL) provides unique insight into the hierarchical assembly process of galaxy clusters. However, the ICL is difficult to study due to its low surface brightness and large physical extent. We present optical spectra of three ICL regions in the Coma cluster, located between 100-180 kpc from their nearest brightest cluster galaxies (BCGs): NGC 4889 and NGC 4874. The mean surface brightness of the three ICL regions are  $\mu_g \approx 25.3 - 26.2$  mag arcsec<sup>-2</sup>. Integral-field unit (IFU) spectroscopy with 13.5 hr on-source integration time were acquired as part of an ancillary program within the SDSS-IV MaNGA survey. We stacked the 127 individual fiber spectra in each IFU in order to achieve a  $1\sigma$  limiting surface brightness of 27.9 mag arcsec<sup>-2</sup>, corresponding to a mean signal-to-noise ratio in the optical of 21.6 Å<sup>-1</sup>, 9.6 Å<sup>-1</sup>, and 11.6 Å<sup>-1</sup>, for each region. We apply stellar population models to the stacked spectra, and measure the recession velocities, velocity dispersions, stellar ages, and metallicities in the three ICL regions. Our results show that the velocity dispersions of ICL regions are very high ( $\sigma \sim 650$  km s<sup>-1</sup>), indicating the stars in these regions are tracing the gravitational potential of the cluster, instead of any individual galaxy. The line-of-sight velocities of the three ICL regions are different from each other by  $\sim 700$  km s<sup>-1</sup>, while the velocity of each region is similar to the closest BCG. This suggests that the ICL regions are associated with two distinct subclusters centered on NGC 4889 and NGC 4874. The stellar populations of these regions are old and metal poor, with ages of  $12.4_{-3.3}^{+1.2}$  Gyr,  $6.6_{-2.4}^{+2.5}$  Gyr, and  $10.6_{-4.3}^{+2.8}$  Gyr, and iron abundances, [Fe/H], of  $-0.8_{-0.3}^{+0.2}$ ,  $-0.6_{-0.5}^{+0.3}$ , and  $-0.8_{-0.3}^{+0.3}$ . From the derived age and metallicity, the build-up of ICL in Coma is likely to be through the accretion of low mass galaxies or the tidal stripping of the outskirts of massive galaxies that have ended their star formation early on, instead of directly from major mergers of massive galaxies.

*Keywords:* galaxies: evolution

### 1. INTRODUCTION

According to the widely accepted  $\Lambda$ -Cold Dark Matter model, massive early type galaxies (ETGs) are assembled hierarchically following their underlying dark matter structures (White & Rees 1978). The evolution of ETGs in massive halos can be described by a two-phase

picture (Naab et al. 2007; Feldmann et al. 2010; Johansson et al. 2012; Navarro-González et al. 2013; Oser et al. 2010, 2012; Qu et al. 2017; Rodriguez-Gomez et al. 2016; Lackner et al. 2012): at high redshift their evolution is dominated by the concentrated mass growth through rapid dissipational in-situ star formation (Daddi et al. 2005; Trujillo et al. 2006; Hopkins et al. 2008; Dekel

et al. 2009; Hyde & Bernardi 2009) At later times, their evolution is increasingly dominated by the build up of the outskirts through multiple mergers and accretions of lower mass galaxies (Ostriker & Tremaine 1975; van der Wel et al. 2014; Bezanson et al. 2009; van Dokkum et al. 2010; van der Wel et al. 2011).

Brightest cluster galaxies (BCGs) are a special class of ETGs residing near the center of galaxy clusters. The most significant structural feature of BCGs is their diffuse and extended stellar envelopes, so they are also classified as cD galaxies. If we trace the stellar distribution from the inner regions of BCGs to the stellar envelopes, part of the stellar components would be no longer bound to the galaxy, but instead associated with the whole cluster as we approach large radius. Many studies have confirmed that in some massive ETGs and BCGs, the stellar velocity dispersion profiles rise with increasing radii towards the velocity dispersion of the cluster (e.g. Faber et al. 1977; Dressler 1979; Kelson et al. 2002; Bender et al. 2015; Veale et al. 2018). The stellar structure surrounding BCGs that are gravitationally bounded to the galaxy cluster is called the intracluster light (ICL) (Zwicky 1951). The formation of the ICL is considered to be a combined effect of multiple mechanisms, including tidal disruption of dwarf galaxies (Rudick et al. 2009), tidal striping of low mass galaxies through galaxy interactions (Conroy et al. 2007; Purcell et al. 2007; Rudick et al. 2009; Contini et al. 2014), violent relaxation during major mergers (Murante et al. 2007), and in-situ star formation (Puchwein et al. 2010). Stellar populations in the outskirts of galaxies and the ICL, if measured, can help constrain these scenarios.

Observing the outskirts of massive ETGs is difficult due to the low surface brightness, but this field has been accelerated by the state of art instruments and improved data reduction in both photometry (van Dokkum et al. 2014; Duc et al. 2015; Mihos et al. 2005; Huang et al. 2016, 2018a,b) and spectroscopy (Sánchez-Blázquez et al. 2007; Foster et al. 2009; Spolaor et al. 2010; Greene et al. 2012, 2015; Coccato et al. 2010, 2011). Observations of the diffuse ICL with extremely low surface brightness is even more challenging. Deep imaging and accurate sky subtraction are required to detect the ICL and constrain their growth over time (Burke et al. 2015; Gonzalez et al. 2005; Rudick et al. 2010; Toledo et al. 2011; Guennou et al. 2012; Giallongo et al. 2014; Mihos et al. 2005; Zibetti et al. 2005). The stellar population and kinematic properties have been explored through multi wavelength photometry (Montes & Trujillo 2014; Williams et al. 2007; Montes & Trujillo 2018), integral-field spectroscopy (Adami et al. 2016; Edwards et al. 2016), globular clusters (Alamo-Martínez & Blakeslee 2017), and individual objects such as planetary nebulae (Arnaboldi et al. 2003, 2004; Gerhard et al. 2007) and red giants branch stars (Feldmeier et al. 2004; Longobardi et al. 2015).

In this paper, we present a stellar population analysis from the BCG centers out to the ICL regime through full spectral modeling, and provide the recession velocity, velocity dispersion, stellar age, and iron abundance out to 180 kpc. This is the first time that the stellar population analysis through full optical spectra modeling is performed beyond 100 kpc. We make use of the data obtained as part of the Deep Coma ancillary program within the SDSS-IV/MaNGA program, and the  $g$  and  $r$  band photometry from the Dragonfly Telephoto Array (Abraham & van Dokkum 2014). The Coma cluster has a median redshift of  $cz = 7090 \text{ km s}^{-1}$  (Geller et al. 1999) and a velocity dispersion of  $\sigma \sim 1000 \text{ km s}^{-1}$  (Colless & Dunn 1996; Mobasher et al. 2001; Rines et al. 2013; Sohn et al. 2016). The distance of Coma Cluster is assumed to be 100.0 Mpc, adopted from Liu & Graham (2001). This corresponds to a distance modulus of 34.99 mag and a scale of  $0.474 \text{ kpc arcsec}^{-1}$ . The Galactic foreground extinction for Coma Cluster is  $A_g = 0.030 \text{ mag}$  and  $A_r = 0.021 \text{ mag}$  (Schlafly & Finkbeiner 2011).

## 2. DATA

### 2.1. Project Overview and Observation Strategy

We make use of data obtained by the MaNGA Survey (Mapping Nearby Galaxies at Apache Point Observatory, (Bundy et al. 2015; Yan et al. 2016; Drory et al. 2015; Wake et al. 2017; Abolfathi et al. 2018). MaNGA is a large, optical integral field spectroscopy survey with 17 deployable integral field units (IFUs) (ranging from 12" to 32" in diameter), and one of the fourth-generation Sloan Digital Sky Survey (SDSS-IV) programs (Gunn et al. 2006; Blanton et al. 2017). The primary goal of MaNGA is to obtain integral field spectroscopy of  $\sim 10,000$  nearby galaxies.

MaNGA utilizes integral field units (IFUs) from two dual-beam Baryonic Oscillation Spectroscopic Survey (BOSS) spectrographs (Drory et al. (2015)) that are on the SDSS 2.5 meter telescope. The spectrographs have 1423 fibers in total that are bundled into different size of IFUs. The diameter of each fiber is  $1.98''$  on the sky. The wavelength coverage of the spectrographs is  $3622 - 10354 \text{ \AA}$  with a  $\sim 400 \text{ \AA}$  overlap from  $\sim 5900$  to  $\sim 6300 \text{ \AA}$  between the blue and red cameras. The spectral resolution is  $R = 1560 - 2650$ .

Our data comes from one of the MaNGA's ancillary programs, the Coma Deep program <sup>1</sup> (also see Gu et al. 2018b). This is the deepest MaNGA ancillary program, consisting of six plates designed to observe specially selected targets in the Coma cluster. The goal of the Coma Deep program is to study the stellar population of various kinds of targets in the Coma cluster and its surrounding area. The plates are  $\sim 0.7$  meter in diameter and  $3^\circ$  on the sky. The center of all plates is at

<sup>1</sup> [www.sdss.org/dr14/manga/manga-target-selection/ancillary-targets/coma](http://www.sdss.org/dr14/manga/manga-target-selection/ancillary-targets/coma)

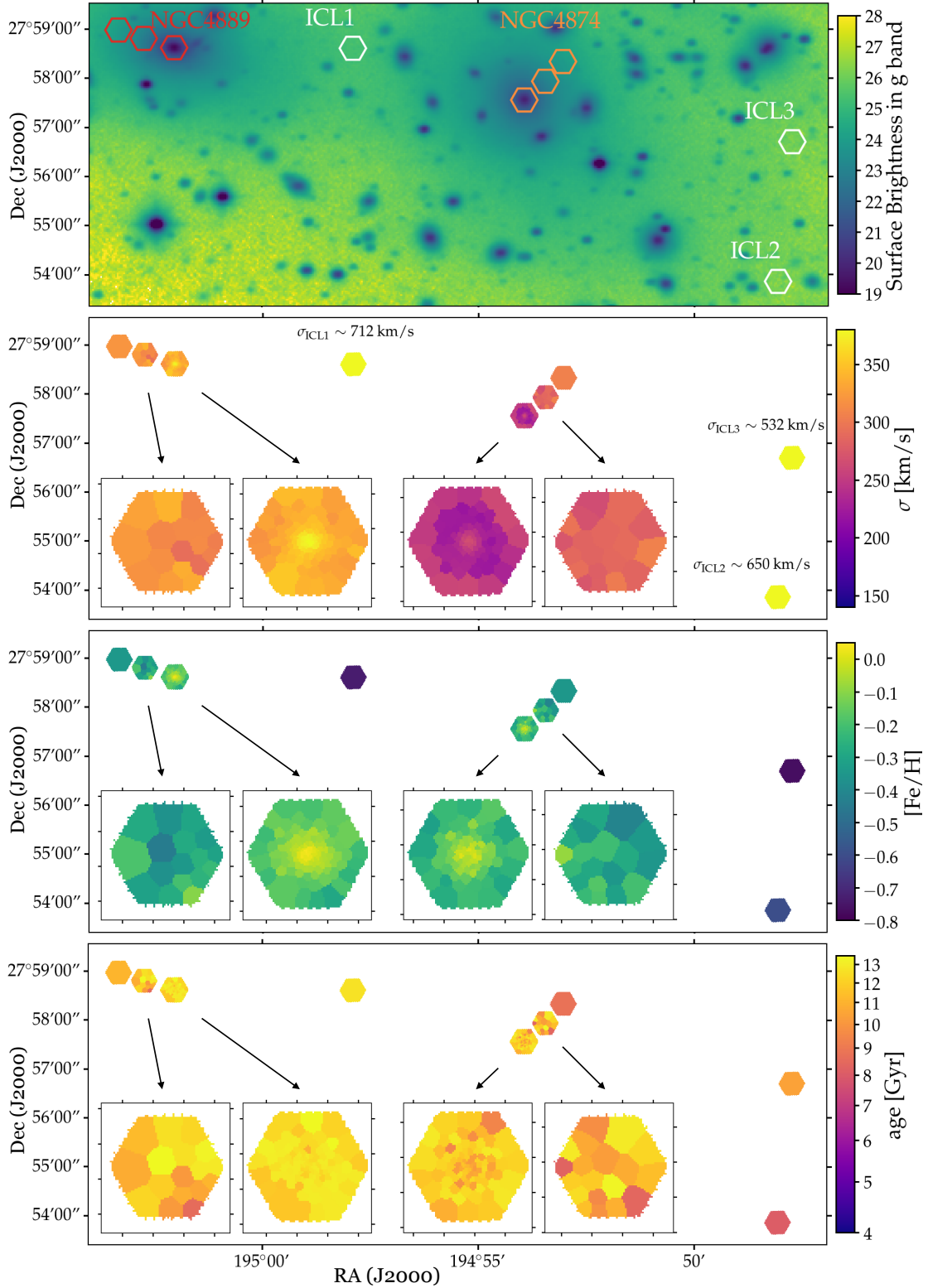


**Figure 1.** First panel: overview of the IFU bundle locations on g-band surface brightness map observed by the Dragonfly Telephoto Array. Red hexagons show IFU locations on the center,  $1R_e$  and  $2R_e$  of NGC 4889. Orange hexagons show IFU locations on the center,  $0.5R_e$ ,  $1R_e$  of NGC 4874. White hexagons show locations of IFUs on ICL1, ICL2, and ICL3, respectively. Second to last panels: spatial distributions of best-fit parameters derived from fitting spatially stacked spectra by `alf`: stellar velocity dispersion  $\sigma$ , iron abundance  $[\text{Fe}/\text{H}]$  and stellar age.

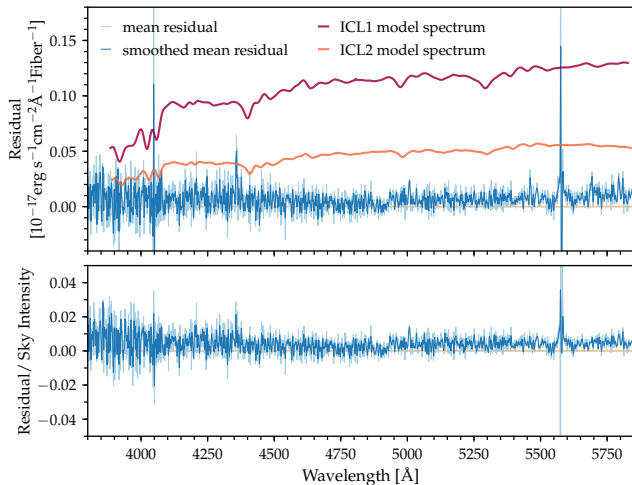


**Figure 2.** Top panel: mean stacked residual of sky-subtracted sky spectra from all science fibers in the nod exposures in which all bundles are placed on background sky (light blue), and that smoothed by a 3-pixel moving box (dark blue). Model spectra of the brightest (ICL1, red) and faintest (ICL2, orange) ICL regions are shown as a noiseless version of the expected target flux level. Bottom panel: fractional residual relative to the sky intensity.

RA=  $12^h58^m35.58^s$ , DEC=  $27^d36^m12.744^s$ . Five massive ETGs are selected for observations: NGC 4889, NGC 4874, NGC 4860, NGC 4839 and NGC 4841A, as well as three dwarf elliptical galaxies: GMP 2232, GMP 5076 and GMP 5361. Observations of massive ETGs are conducted on their central regions and outskirts up to  $\sim 40$  kpc away from the centers. These positions are carefully chosen for optimizing IFU bundle mapping of desired targets. Three 127-fiber bundles are placed in regions of extremely low surface brightness in order to probe the stellar populations of the ICL. These regions are selected based on deep images by the Dragonfly Telephoto Array and are away from any foreground contamination, with a surface brightness in  $g$  band from 25.3 to 26.2 mag arcsec $^{-2}$ . The diameter of each 127-fiber IFU bundle on the sky is  $32''.5$ .

Locations of IFU bundles on two BCGs and three ICL regions are shown in the Dragonfly- $g$  band surface brightness map in Figure 1. The distance from ICL1 to NGC 4889 and NGC 4874 are  $219''.2$  and  $219''.6$ , respectively. The distance from ICL2 and ICL3 to NGC 4874 are  $382''.1$  and  $332''.7$ , respectively.

Two 127-fiber IFUs are used to observe NGC 4889 and NGC 4874. We observed their central regions by the 1st and 2nd Coma plates. We observed  $1R_e$  of NGC 4889 and  $0.5R_e$  of NGC 4874 with the third and fourth Coma plates. They are located  $39''.0$  and  $34''.5$  to the centers, respectively. IFU bundles are placed at  $2R_e$  of NGC 4889 and  $1R_e$  of NGC 4874 in the 5th and 6th plates. The locations to the centers are

$71''.5$ ,  $66''.7$ , respectively. The regions are chosen to best avoid contamination from nearby sources. A similar strategy is adopted for NGC 4860, NGC4839 and NGC 4841A. They are observed by 91-fiber and 61-fiber bundles. Three dwarf elliptical galaxies, GMP 2232, GMP 5076, and GMP 5361 are observed by 37-fiber bundles. The locations of IFU bundles on ICL and dwarf elliptical galaxies are kept the same throughout the six plates, providing the deepest MaNGA observations on single targets.

Since the dark-time sky background at APO is  $\sim 22$  mag arcsec $^{-2}$  in  $g$ -band, excellent sky subtraction is required to probe low surface brightness regions. In Deep Coma plates, the locations of reference sky fibers are carefully selected using broad band images taken by the Dragonfly Telephoto Array, reaching a  $g$ -band surface brightness  $\mu_g > 27.8$  mag arcsec $^{-2}$  for sky fiber locations ( $\sim 3''$  around each fiber) based on the Dragonfly imaging. In addition to the 92 single fibers used to construct the model sky spectrum for ordinary MaNGA plates, three IFU bundles (two 19-fiber bundles, one 37-fiber bundle) were devoted to additional measurements of the sky, hence there are 167 sky fibers in total used across both spectragraphs.

In addition, we adopt an on-and-off nodding strategy to improve the accuracy of the background estimate and to mitigate systematics. By shifting the whole field approximately  $20'$  away, we obtain reference “all-sky” exposures, during which a large fraction of the sky fibers and science IFUs sample the blank sky. Each of the first two plates includes nine 5-minute nodded sky exposures at nine different locations between the normal science exposures. After the first two plates, we decided to change the exposure time to the same as the science exposure in order to better constrain the systematics. Therefore, each of the last four plates includes four 15-minute nodded sky exposures at four different locations.

## 2.2. Data Reduction

We processed the data using a custom modified version of the MaNGA Data Reduction Pipeline MPL-7 (DRP; Law et al. 2015; Law et al. 2016). DRP MPL-7 will be made publicly available in DR15 that is planned for December 2018. The baseline DRP first removes detector overscan regions and quadrant-dependent bias and extracts the spectrum of each fiber using an optimal profile-fitting technique. It uses the sky fibers to create a super-sampled model for the background sky spectrum and subtracts this model spectrum from each of the science fibers. Flux calibration is then performed on individual exposures using 12 7-fiber IFUs targeting spectrophotometric standard stars (Yan et al. 2016; Yan et al. 2016). Fiber spectra from the blue and red cameras are then combined together onto a common logarithmic wavelength solution using a cubic b-spline fit. These “mgCFRAME” files represent spectra of all 1423 MaNGA fibers from a single exposure in

a row-stacked format, where each row corresponds to an individual 1-dimensional fiber spectrum. The logarithmic wavelength grid runs from  $\log \lambda(\text{\AA}) = 3.5589$  to  $\log \lambda(\text{\AA}) = 4.0151$ , which corresponds to 4563 spectral elements from 3621.5960 to 10353.805\AA. In this paper we only use the data taken by the blue spectrograph. This allows us to avoid additional issues associated with the numerous bright atmospheric OH features in the red.

As described in Gu et al. (2018b), our analysis is possible only with exquisite control of detector and instrumental systematics, and therefore some changes to the DRP have been made specifically for the Deep Coma program. Analysis of our nodded all-sky observations showed evidence for low-level systematics in the detector electronics. Therefore we added a step to measure and remove a  $0.5 e^-/\text{pixel}$  offset in bias between the light-sensitive detector pixels and the overscan region, compensating at the same time for a seasonally-dependent  $0.1 e^-/\text{pixel}$  drift in the difference. In addition, the amplifier-dependent gain values tended to drift from one exposure to the next away from nominal at the  $\sim 0.1\%$  level; we added procedures to measure and correct for this effect empirically using the sky fibers in each exposure. Finally, we modified the DRP to be able to apply the flux calibration vector from the nearest ordinary science exposure in time to the nod exposures (for which there are no calibration stars in the 7-fiber mini bundles).

In addition, performance analysis of early observations in the Deep Coma program revealed that scattered light and the extended ( $> 100$  pixel) profile wings of bright galaxies targeted by the Coma program were contaminating the spectra of fainter objects. We therefore redesigned our observing program to consolidate all bright targets (ETGs and dwarf ellipticals) onto one of the two BOSS spectrographs (Smee et al. 2013), and all faint targets (UDGs and ICL) onto the other so that these targets never share a detector.

Although these modifications substantially improve performance for the Deep Coma program relative to the standard DRP, we find that the final stacked science spectra are nonetheless still limited by systematic residuals over wavelength scale  $> 100\text{\AA}$ . These residuals are consistent between stacked science and nodded sky spectra within each plate, possibly due to cartridge-dependent uncertainties in fiber alignment and the detector point-spread function. The offset ranges from 0 to  $10^{-18} \text{erg s}^{-1} \text{cm}^{-2} \text{\AA}^{-1}$ . In the last four plates, we mitigate the impact of these systematics by fitting the stacked spectra of the sky subtracted nodded sky exposures with a 3 degree polynomial from 3836\AA to 5873\AA in the observed frame and subtracting the result from the corresponding science exposures prior to stacking science spectra. The amplitude of the polynomial correction ranges from  $10^{-19}$  to  $10^{-18} \text{erg s}^{-1} \text{cm}^{-2} \text{\AA}^{-1}$  in the continuum, and represents an important correction to the baseline flux level for extremely faint targets. We

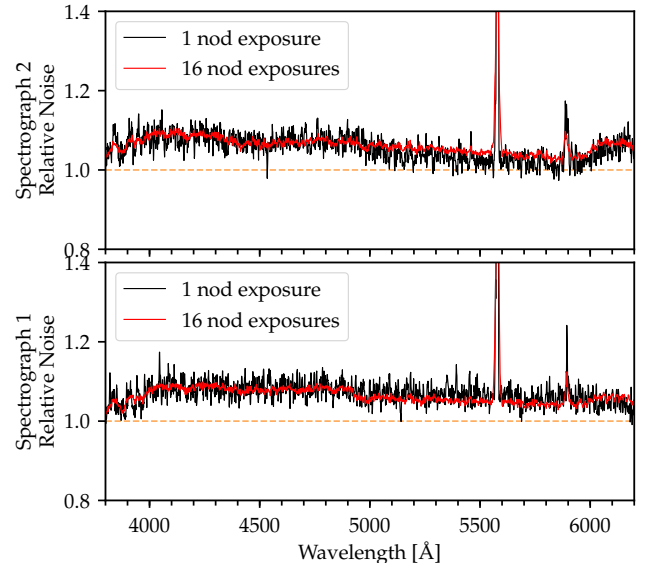


**Figure 3.** Ratio between the actual noise and the expected noise from the detector read noise and Poisson counting statistics as a function of wavelength for the science spectra in one sky subtracted nod exposure (black), and that in all 16 nod exposures (red). The top and bottom panels show results in the first and second spectrograph, respectively. A relative noise of one means perfect, “Poisson limited” sky subtraction (dotted line).

match the continuum levels of stacked spectra from different plates via subtracting the above polynomial continuum before we derive any science result.

### 2.3. Sky Subtraction Performance

We make use of the nodded sky exposures to test the sky subtraction performance we can achieve for the spatially stack ICL spectra. We perform the same analysis on the 15-minute nodded sky exposures in the last four Deep Coma plates, and spatially stack the sky-subtracted sky spectral from all science fibers in these 16 exposures. This provides us an estimate of the sky residual. Figure 2 shows the sky subtracted residual (top panel), and the fractional residual relative to the sky intensity (bottom panel) from the stacked sky-subtracted spectra in nodded sky exposures. Since the number of Deep Coma science exposures is roughly  $3\times$  the number of nodded sky exposures, the residuals are smoothed by a 3-pixel moving box to mimic the residual we could achieve by stacking the same number of nodded sky exposures as the science exposures. They are shown as the dark blue lines. The residuals are very close to zero in the 3800–5800\AA : the wavelength range we used to perform stellar population analysis. The fractional residual relative to the sky intensity is on average within 1%. We further compare the flux level of our science targets, by including model spectra of ICL1 and ICL2 as a noiseless version of the expected flux level. ICL1 and ICL2

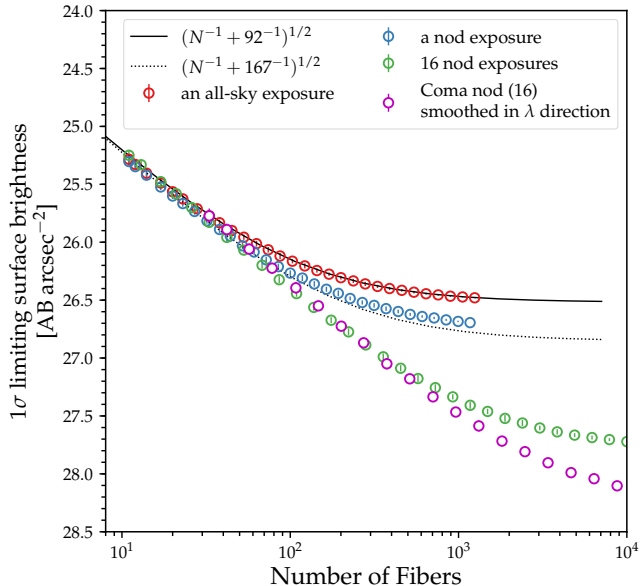


**Figure 4.**  $1\sigma$  limiting surface brightness in the wavelength range  $4000 - 5500\text{\AA}$  as a function of the number of randomly selected and combined fibers in a standard MaNGA all-sky exposure (92 sky fibers, red), a Deep Coma nod exposure (167 sky fibers, blue) and 16 nod exposures (green). The solid and dotted black line shows the theoretical expectation based on  $\sqrt{N^{-1} + 92^{-1}}$  for an all-sky exposure, and  $\sqrt{N^{-1} + 167^{-1}}$  for a nod exposure, respectively. The performance of stacking across all 54 science exposures (purple) is estimated by smoothing the stacked spectrum of all 16 nod exposures by a factor of 3 in the wavelength direction. The sky level in all exposures is  $\sim 22 \text{ mag arcsec}^{-2}$ .

are the brightest and faintest ICL regions, respectively. Figure 2 shows that ICL1 has a flux level much higher than the sky residuals, about  $9\times$  the mean sky residual in the  $3800 - 5800\text{\AA}$ . ICL2 is in general above the mean stacked residual ( $4\times$ ) except for the bright sky lines, which are masked out during our spectral fitting procedure.

We also examine if the sky subtraction is “Poisson limited” by constructing “Poisson ratio” images following the procedures described in Law et al. (2016). The inverse variance in the “mgSFrame” spectra represents the combined effect of shot noise and detector read noise. By comparing the distribution of sky subtracted residual with the expected noise from the detector read noise and Poisson counting statistics, we are able to evaluate the sky subtraction performance in single and multiple exposures. As shown in Figure 3, the distribution of Poisson ratio is slightly above 1.0 but on average smaller than 1.1 at all wavelength, except for the few strongest sky lines. Stacking across multiple exposures does not increase this ratio.

Furthermore, we calculate the  $1\sigma$  limiting surface brightness following the steps in Law et al. (2016). Using

the flux calibrated, camera combined mgCFrame spectra, we calculate the limiting  $1\sigma$  surface brightness in  $4000-5500\text{\AA}$  achieved in the blank sky by randomly stacking different numbers of spectra. The results are shown in Figure 4. For a typical MaNGA all-sky exposure with 92 available sky fibers (red), the performance is limited by the number of sky fibers, therefore decreases as  $\sqrt{N^{-1} + 92^{-1}}$ . For a Coma nodded exposure, there are 167 sky fibers, therefore the  $1\sigma$  limiting surface brightness (blue) follows the curve of  $\sqrt{N^{-1} + 167^{-1}}$ . Stacking across different exposures is more complicated, and we estimate this performance by stacking across all 16 Coma nod exposures (green). We further smoothed the stacked nod exposures in the wavelength direction by a factor of 3 to mimic the  $1\sigma$  limiting surface brightness we are able to achieve by 54 science exposures, which have  $\sim 3\times$  exposures as the nod exposures. With the same number of science fibers as we used in our ICL targets, the  $1\sigma$  limiting surface is about  $28 \text{ mag arcsec}^{-2}$ . Finally, we estimate the  $1\sigma$  limiting surface brightness achieved by stacking all ICL1 fibers in all 54 exposures by first subtracting off a high smoothed continuum model in each spectrum. The  $1\sigma$  limiting surface brightness derived from ICL1,  $27.9 \text{ mag arcsec}^{-2}$ , is a close estimate of the real performance, and is roughly consistent with the predictions from the nodding exposures. Since the surface brightness of three ICL regions is  $\mu_g \approx 25.3 - 26.2$ , they are about at the same level of  $10\sigma$  limiting surface brightness. In summary, we achieve a  $1\sigma$  limiting surface brightness of  $27.9 \text{ mag arcsec}^{-2}$  by spatially stacking the ICL spectra over 54 science exposures for our  $\mu_g \approx 25.3 - 26.2 \text{ mag arcsec}^{-2}$  targets under the  $\mu_g \approx 22 \text{ mag arcsec}^{-2}$  sky background.

### 3. STELLAR POPULATION MODELING

#### 3.1. Absorption Line Fitter

Our main tool for modeling spectra of galaxies and ICL in our sample is the absorption line fitter (alf, Conroy & van Dokkum 2012; Conroy et al. 2014, 2017, 2018). alf enables stellar population modeling of the full spectrum for stellar ages  $> 1\text{Gyr}$  and for metallicities from  $\sim -2.0$  to  $+0.25$ . With alf we explore the parameter space using a Markov Chain Monte Carlo algorithm (emcee, Foreman-Mackey et al. 2013). The program now adopts the MIST stellar isochrones (Choi et al. 2016) and utilizes a new spectral library that includes continuous wavelength coverage from  $0.35 - 2.4\mu\text{m}$  over a wide range in metallicity. This new library, described in Vilaume et al. (2017), is the result of obtaining new IRTF NIR spectra for stars in the MILES optical spectral library (Sánchez-Blázquez et al. 2006). Finally, theoretical response functions, which tabulate the effect on the spectrum of enhancing each of 18 individual elements, were computed using the ATLAS and SYNTH programs (Kurucz 1970, 1993). Further details of these updates to alf are described in Conroy et al. (2018). With

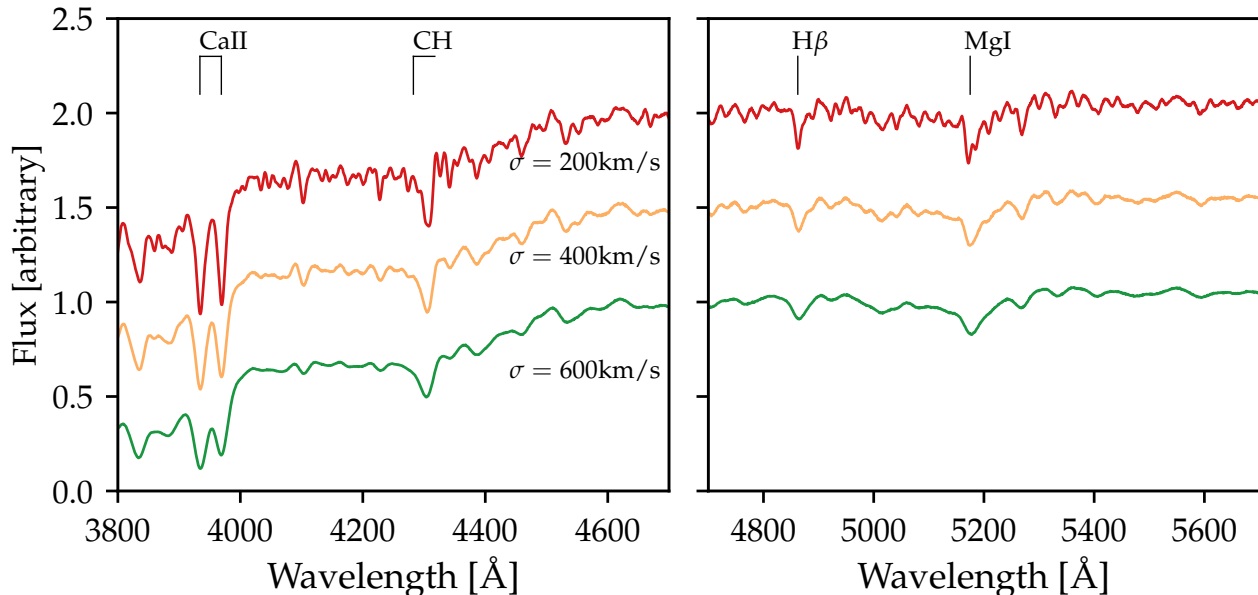


**Figure 5.** Model spectra with different velocity dispersions. Targets with high velocity have much shallower absorption features. Model spectra for a stellar population of age of 10 Gyr and  $[\text{Fe}/\text{H}] = -0.7$ . The spectra in red, orange and green are smoothed with velocity dispersion of 200, 400 and 600  $\text{km s}^{-1}$ . Prominent absorption features in the ICL spectra are labeled.

alf we are able to fit a two burst star formation history, the redshift, velocity dispersion, overall metallicity ( $[\text{Z}/\text{H}]$ ), 18 individual element abundances, several IMF parameters, and a variety of “nuisance” parameters.

Throughout this paper, we use *alf* in a simplified mode. Not all the parameters are included, but only the recession velocity, age, overall metallicity  $[\text{Z}/\text{H}]$  and abundances of Fe, C, N, O, Mg, Si, Ca, Ti, and Na. The IMF is fixed to the Kroupa (2001) form. Instead of adopting a two burst star formation history in the standard model, the simplified mode adopts only a single age component. We adopt this approach due to the limited S/N of the data. We adopt flat priors from 500 – 10500  $\text{km s}^{-1}$  for recession velocity, 10 – 2000  $\text{km s}^{-1}$  for velocity dispersion, 1.0 – 14.0 Gyr for age and  $-1.8 - +0.3$  for  $[\text{Fe}/\text{H}]$ . The priors are zero outside these ranges. For each spectrum, we normalize the continuum by fitting the ratio between model and data in the form of a polynomial. For spectra from IFU bundles that are located within 50 kpc from the centers of BCGs, we use the polynomial with order of  $(\lambda_{max} - \lambda_{min})/100\text{\AA}$ . For ICL targets, due to the large velocity dispersion in the stellar content, we adopt a 6th-order polynomial (see Appendix). For each likelihood evaluation, the polynomial-divided input spectra are matched with the model. normalization occurs in two separate wavelength intervals, 3800 – 4700Å and 4700 – 5600Å. Pixels near bright sky lines in the blue were masked prior to the fitting.

Figure 5 shows model spectra for old and low metallicity stellar populations with the same stellar age of 10 Gyr and  $[\text{Fe}/\text{H}]$  of  $-0.7$ , but different velocity dis-

persions: 200, 400, and 600  $\text{km s}^{-1}$ . For a typical ETG, the velocity dispersion in the central region is roughly 200 – 300  $\text{km s}^{-1}$ . The velocity dispersion in the ICL regions are  $> 400 \text{ km s}^{-1}$ . Compared to typical ETGs, the stellar absorption features in regions with  $> 400 \text{ km s}^{-1}$  become much shallower with increasing velocity dispersion. Therefore ICL spectra are noticeably different than typical ETG spectra.

## 4. RESULTS

### 4.1. Stellar Population of the ICL

We now present our results from full spectra modeling. The total on-source exposure time for each ICL regions is 13.5 hours. The mean S/N ratio we achieved for ICL1, ICL2 and ICL3 in wavelength range from 4500 – 5000Å are  $21.6\text{\AA}^{-1}$ ,  $9.6\text{\AA}^{-1}$ , and  $11.6\text{\AA}^{-1}$ . Figure 6 shows the median stacked spectra for ICL1, ICL2, and ICL3 from the 54 15-minute exposures observed by the six Coma plates (Plate 8479, 8480, 8953, 9051). The spectrum shown in the figure is smoothed by a 3 pixel boxcar kernel. Visually prominent stellar absorption features for old stellar populations have been captured by the best-fit model spectra (red), including Ca II H&K lines, CH, H $\beta$ , and MgI. The red spectrum shows the best fit spectra by *alf*. In Figure 7 we show the projections of posteriors (Foreman-Mackey 2016) for four parameters: recession velocity (*cz*), velocity dispersion,  $\log(\text{age})$  and  $[\text{Fe}/\text{H}]$ . The posterior distributions are well approximated by a Gaussian. Dashed lines show the values of parameters at 16th, 50th and 84th percentiles of posteriors. Blue lines mark the values of parameters at minimum  $\chi^2$ . Outliers are shown as dots.

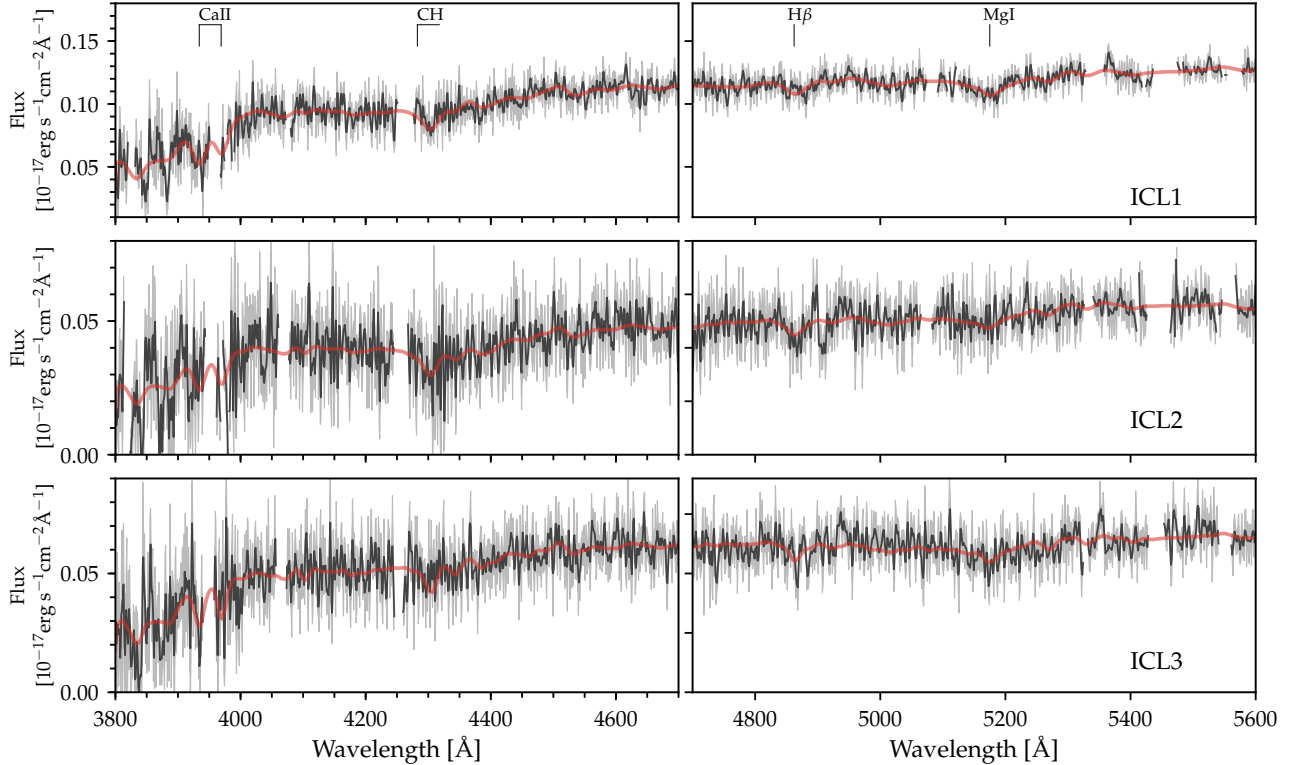


**Figure 6.** Stacked spectra (black) and best-fit model spectra (red) with parameters at minimum  $\chi^2$  from `alf` of ICL1 (top), ICL2 (middle), and ICL3 (bottom). Spectra are smoothed with a 3 pixel box car filter for the purpose of better display. Gray shaded regions show the uncertainty of flux from the input spectra. Gaps in the black lines indicate pixels that are masked prior to the fitting, which are pixels contaminated by bright sky lines.

The Coma cluster has a median redshift of  $cz = 7090 \text{ km s}^{-1}$  (Geller et al. 1999). The recession velocities of ICL1, ICL2, and ICL3 are  $6728_{-133}^{+67} \text{ km s}^{-1}$ ,  $7288_{-72}^{+53} \text{ km s}^{-1}$ , and  $7583_{-20}^{+86} \text{ km s}^{-1}$ , respectively. The derived velocity dispersions confirm that the stellar content in these regions belong to the Coma cluster. All of the three ICL regions have high velocity dispersion:  $712_{-66}^{+114} \text{ km s}^{-1}$ ,  $650_{-94}^{+164} \text{ km s}^{-1}$ ,  $532_{-87}^{+283} \text{ km s}^{-1}$ . The ages of ICL1, ICL2, and ICL3 are  $12.7_{-3.7}^{+1.1} \text{ Gyr}$ ,  $8.1_{-2.9}^{+4.0} \text{ Gyr}$ , and  $10.4_{-4.4}^{+2.9} \text{ Gyr}$ , respectively. The iron abundances,  $[\text{Fe}/\text{H}]$ , are  $-0.74_{-0.25}^{+0.25}$ ,  $-0.59_{-0.42}^{+0.34}$ , and  $-0.77_{-0.29}^{+0.38}$ , respectively. The stellar content in all three ICL regions is old and metal-poor. We note that both the low metallicity and large velocity dispersion lead to less significant absorption features, making it more difficult to extract stellar population properties (see appendix for more detail).

#### 4.2. Surface Brightness and Color Profiles

We derive the surface brightness profiles of NGC 4889 and NGC 4874 by performing the `IRAF`<sup>2</sup> task `ELLIPSE`

<sup>2</sup> STSDAS is a product of the Space Telescope Science Institute, which is operated by AURA for NASA.

(Jedrzejewski 1987) on the sky subtracted Dragonfly images. Surrounding objects are aggressively masked iteratively using `SExtractor` (Bertin & Arnouts 1996). The centers of galaxies are determined first, then the ellipticity and position angle are determined by the median values in radial range 10-100 kpc. We extract the surface brightness profile along the major axis out to 300 kpc with fixed ellipticity and position angle, and correct them for Galactic extinction. Error-bars on the surface brightness and  $g-r$  color profiles are calculated by combining the uncertainty in intensity from the `ELLIPSE` procedure, and the intrinsic fluctuation of the background level obtained from aggressively masked Dragonfly images. The  $g$  band surface brightness and  $g-r$  color profiles of NGC 4889 and NGC 4874 are shown in Figure 9.  $g$  band surface brightness predicted by the best-fit model spectra obtained by spatially stacking spectra in the first two plates, the 3rd and 4th plates, the 5th and 6th plates, and three ICL regions are shown as comparisons. The results from two methods are consistent with each other within  $1\sigma$ . Figure 9 also shows that the  $g-r$  color of three ICL regions inferred from the best-fit `alf` model are consistent with photometry from Dragonfly images. Both BCG+ICL  $g-r$  colors become bluer with increasing radius. This is consistent with our

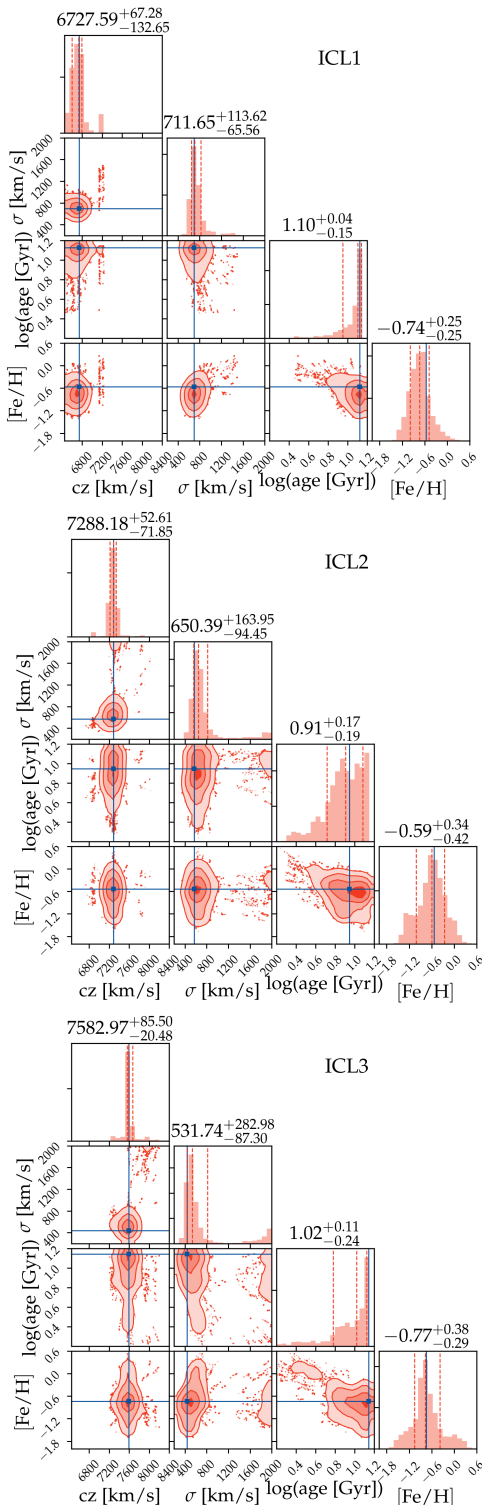


**Figure 7.** Projections of the posterior of recession velocity, velocity dispersion,  $\log(\text{age})$ , and  $[\text{Fe}/\text{H}]$  from `a1f` in 1D and 2D histograms for ICL1, ICL2, and ICL3. Dashed lines and contours show the 16th, 50th and 84th percentiles of posteriors. Blue lines represent the best fit parameters at  $\chi^2_{\text{min}}$ , which are used to generate best-fit model spectra.

spectroscopic results that the stellar population is more metal poor with increasing radius.

### 4.3. Radial Variations

In this section we compare the radial variations in the stellar population properties. We first compare the median spatially stacked spectra among the central region of NGC 4889 and NGC 4874 (1st and 2nd plates), at around  $0.5\text{--}1R_e$  (3rd and 4th plates) and  $1\text{--}2R_e$  (5th and 6th plates), and the ICL regions in Figure 10. Stacked spectra in Figure 6 are smoothed by a 3 pixel wide boxcar kernel, overplot by the best fit model spectra. The absorption features in the ICL spectra are visually shallower than the inner regions of BCGs, suggesting a higher velocity dispersion of stars in the ICL.

The  $g$  band image surface brightness profiles and  $g-r$  color profiles derived from the Dragonfly images are shown in the top panels of Figure 8. We then compare the stellar population properties as a function of radius in the lower four panels of Figure 8, including their recession velocity ( $cz$ ), velocity dispersion ( $\sigma$ ), stellar age and iron abundance  $[\text{Fe}/\text{H}]$ . We also include the radial trends of three massive ETGs in the Coma cluster observed in the Deep Coma program: NGC 4860, NGC 4841A, and NGC 4839. The radial coverage of these three galaxies are  $\sim 0\text{--}30$  kpc. The mean recession velocities of the three ICL regions are very close to their nearest BCGs, NGC 4889 and NGC 4874.

For the velocity dispersion ( $\sigma$ ), stellar age and iron abundance  $[\text{Fe}/\text{H}]$ , a more clear view of the radial trends can be found in Figure 1. To study the spatial distribution of stellar population parameters from the central regions of BCGs to the ICL, we make use of the MaNGA data cube that is rectified spatially in units of  $0.5''$  spatial pixels (spaxels) for the observations of NGC 4889 and NGC 4874 in the first four plates, corresponding to the central regions of the two BCGs,  $0.5R_e$  of NGC 4874, and  $1R_e$  of NGC 4889. Spectra in adjacent spaxels are binned by Voronoi tessellation (Cappellari & Copin 2003). To control the bin size, the S/N achieved in each bin in the central regions of two BCGs are  $210\text{\AA}^{-1}$  and  $180\text{\AA}^{-1}$  for NGC 4889 and NGC 4874, respectively. The S/N achieved in each bin of the data cube on  $1R_e$  of NGC 4889 and  $0.5R_e$  of NGC 4874 are  $120\text{\AA}^{-1}$  and  $100\text{\AA}^{-1}$ , respectively. For the  $2R_e$  of NGC 4889 and  $1R_e$  of NGC 4874, we use the “mgCFRAME” files and spatially stacked all science fibers in the bundles, and achieve a  $S/N \approx 50\text{\AA}^{-1}$ . The 2D spatial distributions of the best-fit  $\sigma$ , age and  $[\text{Fe}/\text{H}]$  are displayed in Figure 1.

Both BCGs+ICL structures have rising velocity dispersion profiles, suggesting that stars in the ICL trace the potential of the Coma cluster instead of any individual galaxy. The stellar ages for the three massive galaxies and two BCG+ICL structures are generally old from the center to the outskirts. This is consistent with previous observations of nearly flat stellar age profiles in ETGs (Greene et al. 2015; Sánchez-Blázquez et al.

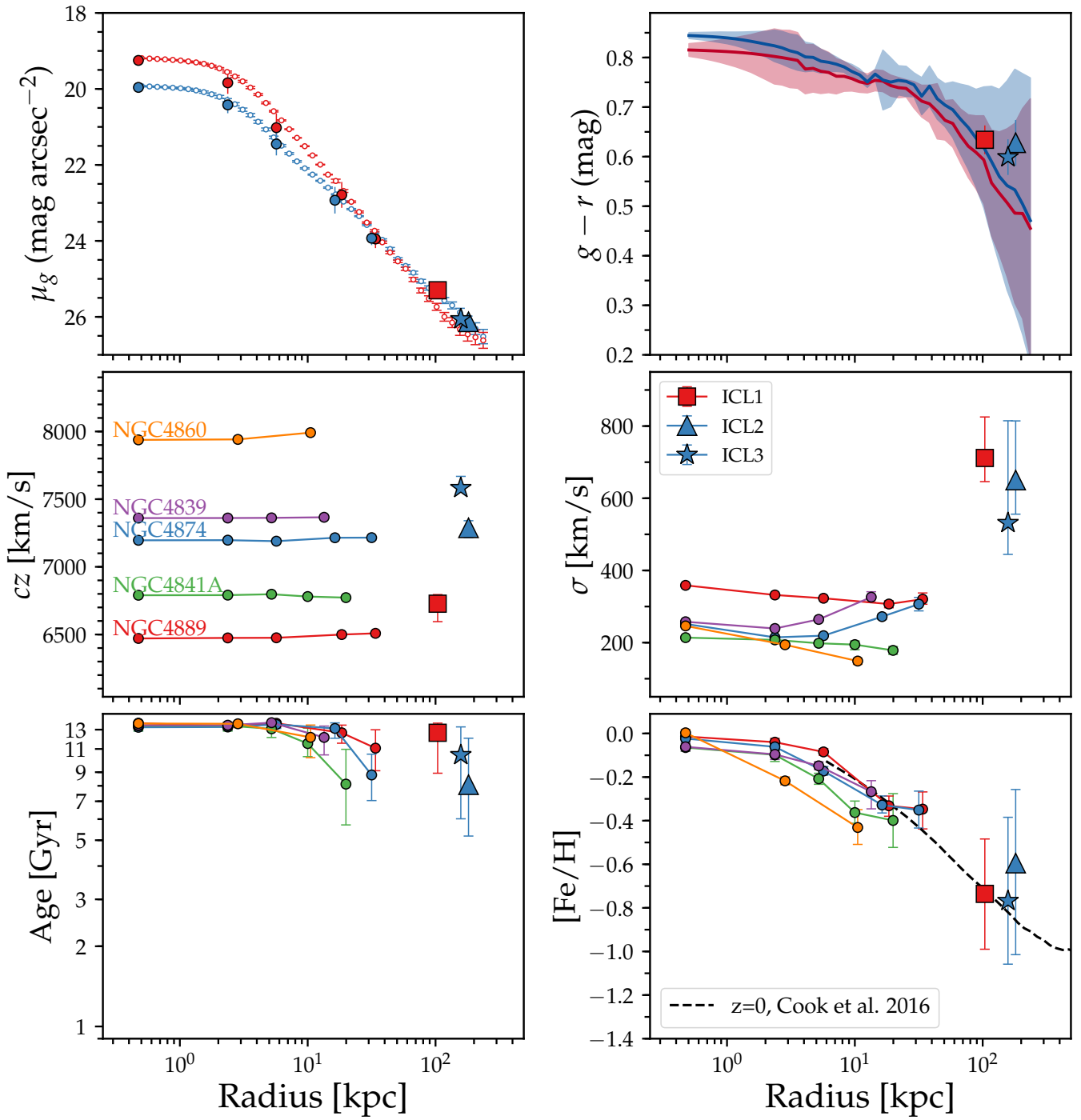


**Figure 8.** Top panels:  $g$ -band surface brightness profiles and  $g - r$  color profiles for NGC 4889 (red) and NGC 4874 (blue), extended into the ICL regime; Middle panels: Best-fit recession velocity  $cz$  and velocity dispersion  $\sigma$  as a function of radius; Bottom panels: Best-fit stellar age and  $[\text{Fe}/\text{H}]$  as a function of radius. Error bars enclose 16th and 84th percentile of the posteriors. Results for ICL regions are marked with the same color as that for their closest BCGs. In the bottom right panel, the dashed line represents the shifted mean metallicity  $[Z/\text{H}]$  profile at  $z = 0$  in  $\log(M_*/M_\odot) \in [11.5, 12.0]$  from the Illustris simulations (Cook et al. 2016). The profile is shifted down by 0.15 dex for reasons explained in the text.

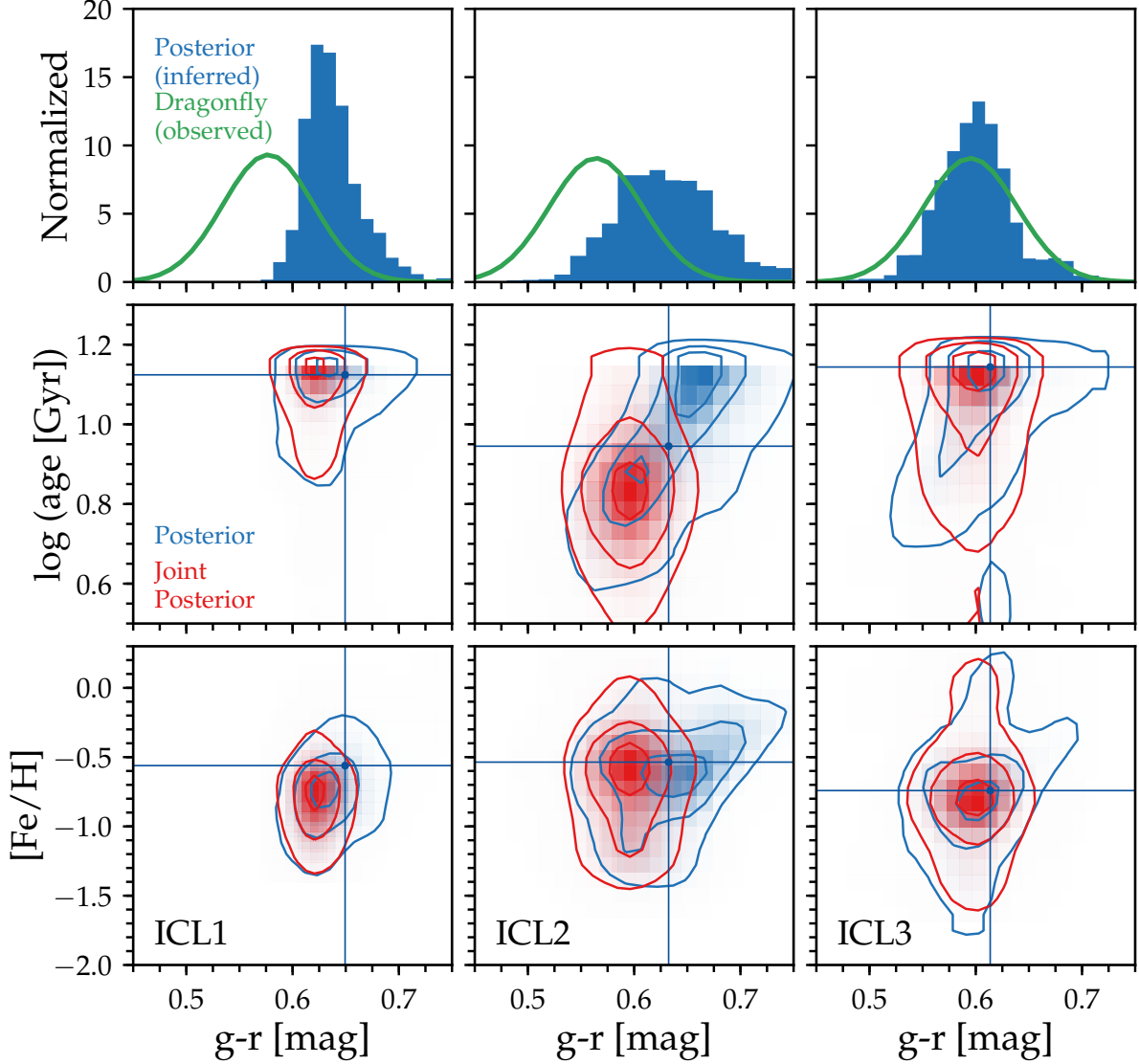


**Figure 9.** Top panel: 1D histogram of inferred  $g - r$  color posterior from `a1f` (blue) for ICL1 (left), ICL2 (middle), and ICL3 (right), compared with the  $g - r$  color from broadband images taken by the Dragonfly Telephoto Array (green). Middle and Bottom panels: Projections of the posterior of  $\log(\text{age})$ ,  $[\text{Fe}/\text{H}]$  and  $g - r$  in 2D histograms. Blue lines show the best fit parameters at  $\chi^2_{\min}$ . The joint posterior distributions from combining broadband colors and model spectra colors are shown in the same panels in red.

2007; Gu et al. 2018a). The stellar age profiles show that both the in-situ and ex-situ components of the massive ETGs in Coma have old stellar populations. The result highlights the effect of “environmental quenching” (Peng et al. 2010), and is consistent with the “coordinated assembly” picture in Gu et al. (2018a) that the massive ETGs in the central regions of galaxy clusters grow by accreting preferentially old stellar systems. In the bottom right panel of Figure 8, we see declining  $[\text{Fe}/\text{H}]$  radial profiles for all of the three massive galaxies and both BCG+ICL structures. The  $[\text{Fe}/\text{H}]$  in the ICL regions are in general even more metal poor than the outskirts of BCGs at  $1-2R_e$ . We compare the radial

profile in the outskirts of two BCG+ICL structures in our sample with the prediction from the Illustris simulations (Cook et al. 2016). The black dashed line in this panel shows the shifted mean projected profiles of  $[\text{Z}/\text{H}]$  in  $z = 0$  galaxies that are in the stellar mass bins of  $\log(M_*/M_\odot) \in [11.5, 12.0)$ . Note that we shift the mean profile since we are comparing only the gradients in the outskirts, and we need to account for the difference between the total metallicity in the simulation and the  $[\text{Fe}/\text{H}]$  in observations. The mean projected profiles of  $[\text{Z}/\text{H}]$  in the Illustris simulations is shifted down by 0.15 dex to match the  $[\text{Fe}/\text{H}]$  at 10 kpc. This difference

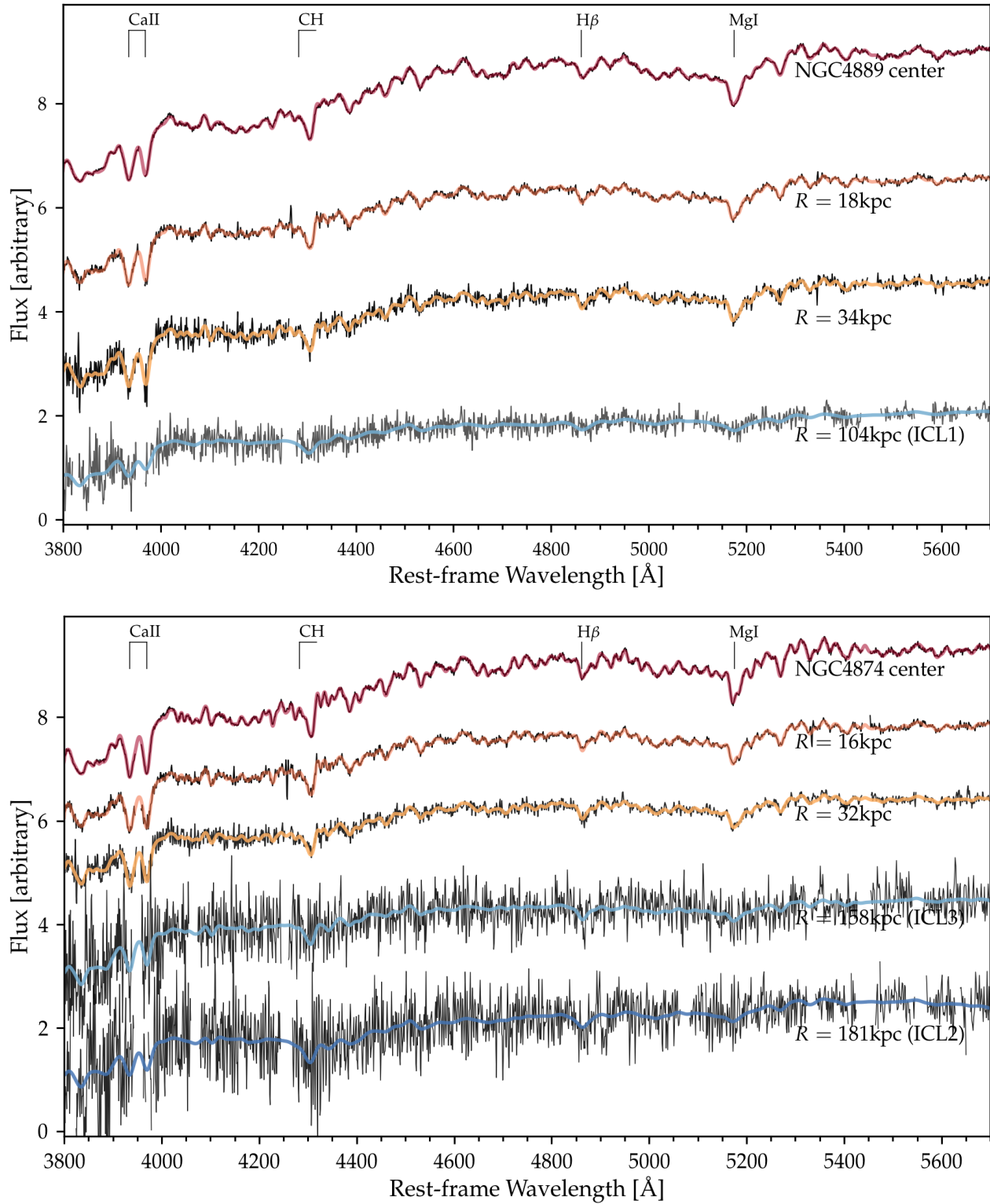


**Figure 10.** Normalized median stacked spectra (black) at different distances to the centers of NGC 4889 (top panel) and NGC 4874 (bottom). Strong absorption features are labeled. Best-fit model spectra with parameters at minimum  $\chi^2$  are shown in colors.

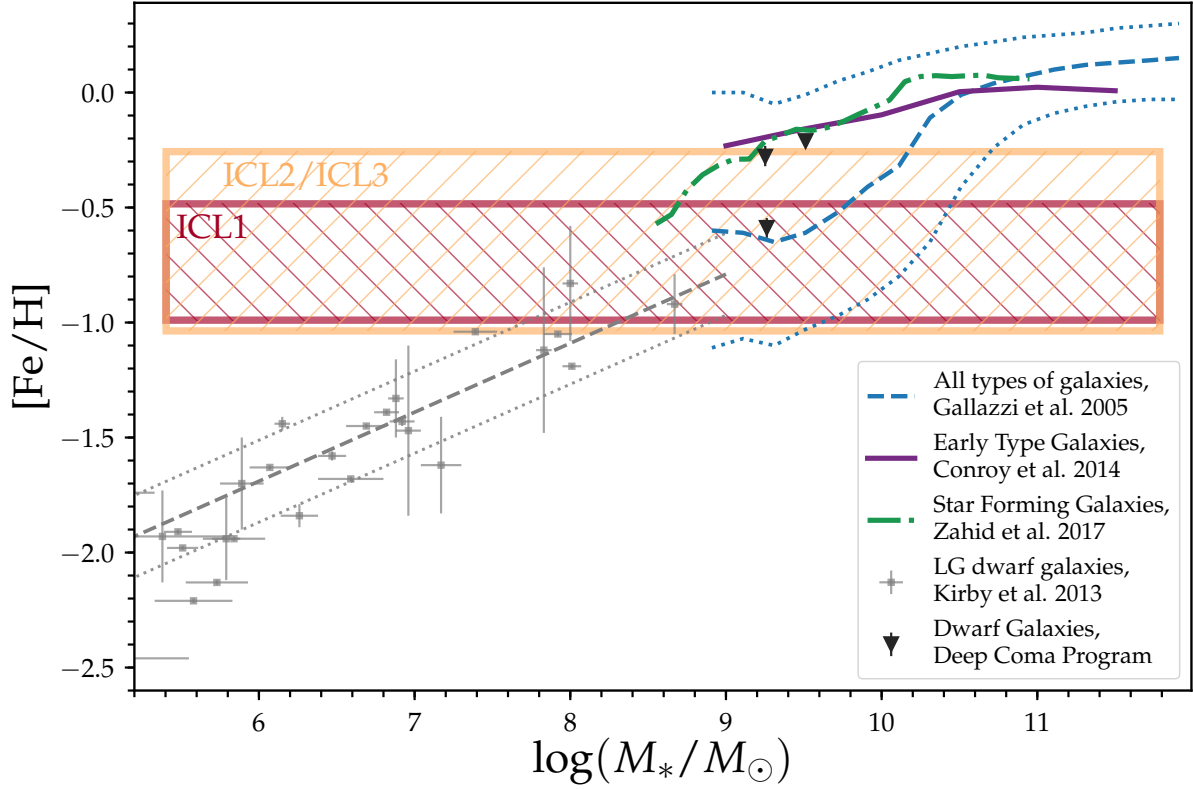


**Figure 11.** Relation between stellar mass and  $[\text{Fe}/\text{H}]$  for three dwarf elliptical galaxies in the Coma cluster (triangles), and previous results from the literature: gray symbols show Local Group dwarf galaxies from Kirby et al. (2013), and gray dashed and dotted lines represent the median, 16th, and 84th percentiles of the metallicity distributions. Blue dashed and dotted lines show the median, 16th, and 84th percentiles of the metallicity distributions for various types of galaxies in Gallazzi et al. (2005). The purple line shows the stellar mass-metallicity relation for early-type galaxies binned in stellar mass (Conroy et al. 2014). The green line represents the relation for star-forming galaxies in SDSS (Zahid et al. 2017). For the three ICL regions in the Coma cluster without stellar mass constraints, their median, 16th and 84th percentiles of  $[\text{Fe}/\text{H}]$  are shown as horizontal region.

accounts for the difference between total metallicity and  $[\text{Fe}/\text{H}]$ .

#### 4.4. Combined Constraints from Spectra and Photometry

The broadband  $g-r$  color obtained from the Dragonfly Telephoto Array is used as an additional constraint to the stellar age and  $[\text{Fe}/\text{H}]$ . We measure the color from the Dragonfly data within an aperture of  $D = 32''$ , similar to the regions of our stacked spectra. The measured  $g-r$  colors are corrected for Galactic extinction. They are  $0.58 \pm 0.04$  mag,  $0.56 \pm 0.04$  mag, and  $0.60 \pm 0.04$  mag for ICL1, ICL2, and ICL3, respectively. We assume the probability density of the observed  $g-r$  colors to be a normal distribution and take the measured color and uncertainty as the mean and standard deviation. The color distributions from Dragonfly photometry are shown in green in the top panels of Figure 9. Normalized 1D posterior distributions of the  $g-r$  color derived from fitting the continuum-normalized spectra are shown in the top panels in blue. The differences are within  $1\sigma$  photometric uncertainty. We then re-weight

the MCMC chains based on the probability density of the broadband  $g-r$  color, and generate new posterior distributions by bootstrap resampling. The middle and bottom panels of Figure 9 show the joint posterior distributions of  $\log(\text{age}/\text{Gyr})$  and  $[\text{Fe}/\text{H}]$  in red, respectively. Slightly tighter constraints are achieved for ICL1 and ICL3. The jointly constrained stellar ages of ICL1, ICL2, and ICL3 are  $12.4^{+1.2}_{-3.4}$  Gyr,  $6.6^{+2.5}_{-2.4}$  Gyr, and  $10.6^{+2.8}_{-4.4}$  Gyr, while the jointly constrained  $[\text{Fe}/\text{H}]$  are  $-0.79^{+0.21}_{-0.25}$ ,  $-0.64^{+0.30}_{-0.45}$ , and  $-0.79^{+0.32}_{-0.31}$ , respectively. Note that derived parameters only change in the case of the stellar age of ICL2.

#### 4.5. Dynamical Structure

The Coma cluster is known to have a complex structure (Mellier et al. 1988; Fitchett & Webster 1987). Previous works found major substructures around the bright galaxy NGC 4839, indicating that there is continuing infall at the present day (Fitchett & Webster 1987; Colless & Dunn 1996; Neumann et al. 2001, 2003). Furthermore, the core of the cluster comprises two giant cD

galaxies, NGC 4889 and NGC 4874, and Xray observations (Adami et al. 2005) suggest that these galaxies are likely associated with two distinct substructures. The line-of-sight velocity distributions of intracluster planetary nebulae in the central region of Coma (Gerhard et al. 2007) also suggest an ongoing merger of distinct substructures associated with NGC 4889 and NGC 4874. Our results contribute to this picture with direct kinematic evidence that the core of Coma is, in fact, a double cluster with two distinct virialized components. The high velocity dispersions in the three ICL regions indicate that the stars in the ICL trace the gravitational potential of subclusters, not galaxies. However, the recession velocities are consistent with those of the two BCGs, with the difference in velocity between ICL1 and ICL2/ICL3 are  $\Delta cz \approx 560 - 850 \text{ km s}^{-1}$ . This shows that stars in ICL1 are tracing a massive dark matter halo around NGC 4889, while stars in ICL2 and ICL3 are tracing a distinct halo around NGC 4874. Our results confirm that NGC 4889 and NGC 4874 not only originate in separate clusters, but that those clusters are still distinct at the present day.

## 5. DISCUSSION

The stellar population in the outskirts of galaxies and the ICL contains important clues related to galaxy accretion and dynamical evolution. Simulations predict that ex-situ mergers are a major contributor to the diffuse light component, and its contribution to the outskirts and ICL regions are more significant for more massive galaxies (Cooper et al. 2013; Lackner et al. 2012; Qu et al. 2017). For example, the IllustrisTNG simulations (Pillepich et al. 2018) predict that a large fraction of stars ( $> 50\%$ ) in the outskirts of massive ETGs ( $> 30 \text{ kpc}$ ) are formed ex-situ. This fraction is even larger ( $\sim 90\%$ ) for stars beyond  $100 \text{ kpc}$ . The radial profile of surface brightness and metallicity of galaxies provide us important clues to their accretion histories. For example, tidally stripped stars at large radii are expected to flatten metallicity and surface brightness profiles (Di Matteo et al. 2009; Vogelsberger et al. 2014; Genel et al. 2014; Cook et al. 2016). Cook et al. (2016) shows that in the Illustris Simulations, the radial profiles of metallicity and surface brightness flatten from  $z = 1$  to the current epoch due to the accretion of stars into the outskirts of galaxies. We compare radial trends of the Coma BCG+ICL structures with the simulations. Despite the large uncertainties of metallicity in the ICL regions, the radial of  $[\text{Fe}/\text{H}]$  trends at  $100\text{-}200 \text{ kpc}$  is consistent with the prediction from simulations.

If the light at  $100 - 200 \text{ kpc}$  is indeed dominated by ex-situ components as predicted by the simulations (e.g. Pillepich et al. 2018), stellar populations in the ICL regions can shed light on the progenitors of ICL. ETGs experienced complex assembly histories, however, they obey tight scaling relations, including the relation between the stellar mass and stellar metallicity, which pro-

vides important clues to their star formation and chemical enrichment history (Lu et al. 2017; Ma et al. 2016; Kirby et al. 2013). By comparing the  $[\text{Fe}/\text{H}]$  of ICL we can infer their possible progenitors. Figure 11 shows the relation between stellar mass and stellar metallicity (MZR). In Figure 11, we draw a horizontal region across nearly all stellar mass with the vertical range covering the 18th and 84th percentiles of  $[\text{Fe}/\text{H}]$  in three ICL regions. The  $[\text{Fe}/\text{H}]$  of the ICL is compared to other populations, including three dwarf elliptical galaxies in the Coma cluster in our sample, ETGs stacked in stellar mass bins (Conroy et al. 2014), star-forming galaxies in SDSS (Zahid et al. 2017), and the MZR from (Gallazzi et al. 2005), which covers both star-forming and quiescent SDSS galaxies, and dwarf galaxies in the Local Group (Kirby et al. 2013). Data points from Gallazzi et al. (2005) and Zahid et al. (2017) represent the total metallicity instead of iron abundances. Note that for the more massive galaxies, the figure shows the relation between their stellar mass and  $[\text{Fe}/\text{H}]$  or total metallicity in the inner region.

The  $[\text{Fe}/\text{H}]$  of ICL regions are similar to the  $[\text{Fe}/\text{H}]$  of three dwarf elliptical galaxies in the Coma cluster. If we estimate the stellar mass of the ICL progenitors based on the MZR, and assume the progenitors have early truncated star formation histories as indicated by the stellar age of three ICL regions, the stellar mass of possible progenitors cover a wide range from  $\sim 10^8 M_\odot$  to  $3 \times 10^9 M_\odot$ . The total ICL stellar mass is  $\approx 10^{12} M_\odot$ , therefore the BCGs would need to merger with  $3 \times 10^3 - 10^4$  such dwarf galaxies if they are the only contributors. Considering we are comparing with the  $[\text{Fe}/\text{H}]$  in the galaxy centers, and their outskirts in general have lower  $[\text{Fe}/\text{H}]$ , it is likely that the stars of the ICL come partly from the outskirts of more massive galaxies. Therefore, the build up of ICL could be from partial tidal stripping of massive galaxies, and/or the disruption of dwarf galaxies with stellar mass above  $\sim 10^8 M_\odot$ . But it is unlikely that the ICL form directly from major mergers of massive galaxies.

The ICL1 spectrum is located between NGC 4889 and NGC 4874. Using a spectral model with a single velocity component, we cannot rule out the possibility that the stellar contents in ICL1 consist of two velocity components, both with lower velocity dispersion. With higher S/N data, we should be able to fit the spectra with a two component model to confirm our conclusion.

## 6. SUMMARY

We have presented the stellar population analysis through full optical spectral modeling for three ICL regions in the Coma cluster that are located between  $100\text{-}200 \text{ kpc}$  from their nearest BCGs. We have measured their recession velocities, velocity dispersion, stellar ages, and iron abundances using spectra obtained as part of the Deep Coma Program within the SDSS-IV/MaNGA survey. Based on their line-of-sight ve-

locity and velocity dispersion, the three ICL regions are associated with two distinct subclusters centered on NGC 4889 and NGC 4874. For the BCG+ICL structures, the radial profiles of stellar age are old and flat, and the radial profiles of [Fe/H] decline with increasing radius. The stellar populations in the ICL regions are all old and metal-poor. The [Fe/H] of three ICL regions are slightly more metal poor compared to the outskirts (10–30 kpc) of massive ETGs in the Coma cluster. From the derived stellar age and metallicity, the build-up of ICL is likely to be through the accretion of low mass galaxies that have ended their star formation early on, or partial tidal stripping of massive galaxies, instead of major mergers of massive galaxies.

M.G. acknowledges support from the National Science Foundation Graduate Research Fellowship. C.C. acknowledges support from NASA grant NNX15AK14G, NSF grant AST-1313280, and the Packard Foundation. MAB. acknowledges NSF Award AST-1517006. The computations in this paper were run on the Odyssey cluster supported by the FAS Division of Science, Research Computing Group at Harvard University.

Funding for the Sloan Digital Sky Survey IV has been provided by the Alfred P. Sloan Foundation, the U.S. Department of Energy Office of Science, and the Participating Institutions. SDSS-IV acknowledges support and

resources from the Center for High-Performance Computing at the University of Utah. The SDSS website is [www.sdss.org](http://www.sdss.org).

SDSS-IV is managed by the Astrophysical Research Consortium for the Participating Institutions of the SDSS Collaboration including the Brazilian Participation Group, the Carnegie Institution for Science, Carnegie Mellon University, the Chilean Participation Group, the French Participation Group, Harvard-Smithsonian Center for Astrophysics, Instituto de Astrofísica de Canarias, The Johns Hopkins University, Kavli Institute for the Physics and Mathematics of the Universe (IPMU) / University of Tokyo, Lawrence Berkeley National Laboratory, Leibniz Institut für Astrophysik Potsdam (AIP), Max-Planck-Institut für Astronomie (MPIA Heidelberg), Max-Planck-Institut für Astrophysik (MPA Garching), Max-Planck-Institut für Extraterrestrische Physik (MPE), National Astronomical Observatories of China, New Mexico State University, New York University, University of Notre Dame, Observatório Nacional / MCTI, The Ohio State University, Pennsylvania State University, Shanghai Astronomical Observatory, United Kingdom Participation Group, Universidad Nacional Autónoma de México, University of Arizona, University of Colorado Boulder, University of Oxford, University of Portsmouth, University of Utah, University of Virginia, University of Washington, University of Wisconsin, Vanderbilt University, and Yale University.

## REFERENCES

- Abolfathi, B., Aguado, D. S., Aguilar, G., et al. 2018, *ApJS*, 235, 42
- Abraham, R. G., & van Dokkum, P. G. 2014, *Publications of the Astronomical Society of the Pacific*, 126, 55
- Adami, C., Biviano, A., Durret, F., & Mazure, A. 2005, *A&A*, 443, 17
- Adami, C., Pompei, E., Sadibekova, T., et al. 2016, *A&A*, 592, A7
- Alamo-Martínez, K. A., & Blakeslee, J. P. 2017, *ApJ*, 849, 6
- Arnaboldi, M., Gerhard, O., Aguerri, J. A. L., et al. 2004, *ApJ*, 614, L33
- Arnaboldi, M., Freeman, K. C., Okamura, S., et al. 2003, *The Astronomical Journal*, 125, 514
- Bender, R., Kormendy, J., Cornell, M. E., & Fisher, D. B. 2015, *ApJ*, 807, 56
- Bertin, E., & Arnouts, S. 1996, *Astronomy and Astrophysics Supplement Series*, 117, 393
- Bezanson, R., van Dokkum, P. G., Tal, T., et al. 2009, *ApJ*, 697, 1290
- Blanton, M. R., Bershady, M. A., Abolfathi, B., et al. 2017, *The Astronomical Journal*, 154, 28
- Bundy, K., Bershady, M. A., Law, D. R., et al. 2015, *The Astrophysical Journal Letters*, 798, 7
- Burke, C., Hilton, M., & Collins, C. 2015, *MNRAS*, 449, 2353
- Cappellari, M., & Copin, Y. 2003, *Monthly Notices of the Royal Astronomical Society*, 342, 345
- Choi, J., Dotter, A., Conroy, C., et al. 2016, *ApJ*, 823, 102
- Coccatto, L., Gerhard, O., & Arnaboldi, M. 2010, *MNRAS*, 407, L26
- Coccatto, L., Gerhard, O., Arnaboldi, M., & Ventimiglia, G. 2011, *A&A*, 533, A138
- Colless, M., & Dunn, A. M. 1996, *The Astrophysical Journal Letters*, 458, 435
- Conroy, C., Graves, G. J., & van Dokkum, P. G. 2014, *The Astrophysical Journal Letters*, 780, 33
- Conroy, C., & van Dokkum, P. 2012, *The Astrophysical Journal Letters*, 747, 69
- Conroy, C., van Dokkum, P. G., & Villaume, A. 2017, *ApJ*, 837, 166
- Conroy, C., Villaume, A., van Dokkum, P. G., & Lind, K. 2018, *ApJ*, 854, 139

- Conroy, C., Wechsler, R. H., & Kravtsov, A. V. 2007, *ApJ*, 668, 826
- Contini, E., De Lucia, G., Villalobos, Á., & Borgani, S. 2014, *MNRAS*, 437, 3787
- Cook, B. A., Conroy, C., Pillepich, A., Rodriguez-Gomez, V., & Hernquist, L. 2016, *ApJ*, 833, 158
- Cooper, A. P., D'Souza, R., Kauffmann, G., et al. 2013, *MNRAS*, 434, 3348
- Daddi, E., Renzini, A., Pirzkal, N., et al. 2005, *ApJ*, 626, 680
- Dekel, A., Sari, R., & Ceverino, D. 2009, *ApJ*, 703, 785
- Di Matteo, P., Pipino, A., Lehnert, M. D., Combes, F., & Semelin, B. 2009, *A&A*, 499, 427
- Dressler, A. 1979, *The Astrophysical Journal Letters*, 231, 659
- Drory, N., MacDonald, N., Bershady, M. A., et al. 2015, *The Astronomical Journal*, 149, 77
- Duc, P.-A., Cuillandre, J.-C., Karabal, E., et al. 2015, *MNRAS*, 446, 120
- Edwards, L. O. V., Alpert, H. S., Trierweiler, I. L., Abraham, T., & Beizer, V. G. 2016, *MNRAS*, 461, 230
- Faber, S. M., Burstein, D., & Dressler, A. 1977, *The Astronomical Journal*, 82, 941
- Feldmann, R., Carollo, C. M., Mayer, L., et al. 2010, *arXiv*, 709, 218
- Feldmeier, J. J., Mihos, J. C., Morrison, H. L., et al. 2004, *ApJ*, 609, 617
- Fitchett, M., & Webster, R. 1987, *ApJ*, 317, 653
- Foreman-Mackey, D. 2016, *The Journal of Open Source Software*, 24, doi:10.21105/joss.00024
- Foreman-Mackey, D., Hogg, D. W., Lang, D., & Goodman, J. 2013, *Publications of the Astronomical Society of the Pacific*, 125, 306
- Foster, C., Proctor, R. N., Forbes, D. A., et al. 2009, *MNRAS*, 400, 2135
- Gallazzi, A., Charlot, S., Brinchmann, J., White, S. D. M., & Tremonti, C. A. 2005, *Monthly Notices of the Royal Astronomical Society*, 362, 41
- Geller, M. J., Diaferio, A., & Kurtz, M. J. 1999, *The Astrophysical Journal Letters*, 517, L23
- Genel, S., Vogelsberger, M., Springel, V., et al. 2014, *MNRAS*, 445, 175
- Gerhard, O., Arnaboldi, M., Freeman, K. C., et al. 2007, *Astronomy & Astrophysics*, 468, 815
- Giallongo, E., Menci, N., Grazian, A., et al. 2014, *ApJ*, 781, 24
- Gonzalez, A. H., Zabludoff, A. I., & Zaritsky, D. 2005, *ApJ*, 618, 195
- Greene, J. E., Janish, R., Ma, C.-P., et al. 2015, *ApJ*, 807, 11
- Greene, J. E., Murphy, J. D., Comerford, J. M., Gebhardt, K., & Adams, J. J. 2012, *ApJ*, 750, 32
- Gu, M., Conroy, C., & Brammer, G. 2018a, *The Astrophysical Journal Letters*, 862, L18
- Gu, M., Conroy, C., Law, D., et al. 2018b, *ApJ*, 859, 37
- Guennou, L., Adami, C., Da Rocha, C., et al. 2012, *A&A*, 537, A64
- Gunn, J. E., Siegmund, W. A., Mannery, E. J., et al. 2006, *AJ*, 131, 2332
- Hopkins, P. F., Hernquist, L., Cox, T. J., Dutta, S. N., & Rothberg, B. 2008, *ApJ*, 679, 156
- Huang, S., Ho, L. C., Peng, C. Y., Li, Z.-Y., & Barth, A. J. 2016, *ApJ*, 821, 114
- Huang, S., Leauthaud, A., Greene, J. E., et al. 2018a, *MNRAS*, 475, 3348
- Huang, S., Leauthaud, A., Greene, J., et al. 2018b, *MNRAS*, 480, 521
- Hyde, J. B., & Bernardi, M. 2009, *MNRAS*, 394, 1978
- Jedrzejewski, R. I. 1987, *Monthly Notices of the Royal Astronomical Society*, 226, 747
- Johansson, P. H., Naab, T., & Ostriker, J. P. 2012, *arXiv*, 754, 115
- Kelson, D. D., Zabludoff, A. I., Williams, K. A., et al. 2002, *The Astrophysical Journal Letters*, 576, 720
- Kirby, E. N., Cohen, J. G., Guhathakurta, P., et al. 2013, *ApJ*, 779, 102
- Kroupa, P. 2001, *Monthly Notices of the Royal Astronomical Society*, 322, 231
- Kurucz, R. L. 1970, *SAO Special Report*, 309
- . 1993, *Kurucz CD-ROM*, Cambridge, MA: Smithsonian Astrophysical Observatory, —c1993, December 4, 1993
- Lackner, C. N., Cen, R., Ostriker, J. P., & Joung, M. R. 2012, *Monthly Notices of the Royal Astronomical Society*, 425, 641
- Law, D. R., Yan, R., Bershady, M. A., et al. 2015, *AJ*, 150, 19
- Law, D. R., Cherinka, B., Yan, R., et al. 2016, *The Astronomical Journal*, 152, 83
- Longobardi, A., Arnaboldi, M., Gerhard, O., & Mihos, J. C. 2015, *A&A*, 579, L3
- Lu, Y., Benson, A., Wetzel, A., et al. 2017, *ApJ*, 846, 66
- Ma, X., Hopkins, P. F., Kasen, D., et al. 2016, *Monthly Notices of the Royal Astronomical Society*, 459, 3614
- Mellier, Y., Mathez, G., Mazure, A., Chauvineau, B., & Proust, D. 1988, *A&A*, 199, 67
- Mihos, J. C., Harding, P., Feldmeier, J., & Morrison, H. 2005, *ApJL*, 631, L41
- Mobasher, B., Bridges, T. J., Carter, D., et al. 2001, *ASTROPHYS J SUPPL S*, 137, 279
- Montes, M., & Trujillo, I. 2014, *ApJ*, 794, 137

- . 2018, *MNRAS*, 474, 917
- Murante, G., Giovalli, M., Gerhard, O., et al. 2007, *MNRAS*, 377, 2
- Naab, T., Johansson, P. H., Ostriker, J. P., & Efstathiou, G. 2007, *ApJ*, 658, 710
- Navarro-González, J., Ricciardelli, E., Quilis, V., & Vazdekis, A. 2013, arXiv, 436, 3507
- Neumann, D. M., Lumb, D. H., Pratt, G. W., & Briel, U. G. 2003, *A&A*, 400, 811
- Neumann, D. M., Arnaud, M., Gastaud, R., et al. 2001, *A&A*, 365, L74
- Oser, L., Naab, T., Ostriker, J. P., & Johansson, P. H. 2012, *ApJ*, 744, 63
- Oser, L., Ostriker, J. P., Naab, T., Johansson, P. H., & Burkert, A. 2010, *ApJ*, 725, 2312
- Ostriker, J. P., & Tremaine, S. D. 1975, *The Astrophysical Journal Letters*, 202, L113
- Peng, Y.-j., Lilly, S. J., Kovac, K., et al. 2010, *The Astrophysical Journal Letters*, 721, 193
- Pillepich, A., Nelson, D., Hernquist, L., et al. 2018, *Monthly Notices of the Royal Astronomical Society*, 475, 648
- Puchwein, E., Springel, V., Sijacki, D., & Dolag, K. 2010, *MNRAS*, 406, 936
- Purcell, C. W., Bullock, J. S., & Zentner, A. R. 2007, *ApJ*, 666, 20
- Qu, Y., Helly, J. C., Bower, R. G., et al. 2017, arXiv, 464, 1659
- Rines, K., Geller, M. J., Diaferio, A., & Kurtz, M. J. 2013, *The Astrophysical Journal Letters*, 767, 15
- Rodriguez-Gomez, V., Pillepich, A., Sales, L. V., et al. 2016, arXiv, 458, 2371
- Rudick, C. S., Mihos, J. C., Frey, L. H., & McBride, C. K. 2009, *ApJ*, 699, 1518
- Rudick, C. S., Mihos, J. C., Harding, P., et al. 2010, *ApJ*, 720, 569
- Sánchez-Blázquez, P., Forbes, D. A., Strader, J., Brodie, J., & Proctor, R. 2007, *MNRAS*, 377, 759
- Sánchez-Blázquez, P., Peletier, R. F., Jiménez-Vicente, J., et al. 2006, *Monthly Notices of the Royal Astronomical Society*, 371, 703
- Smee, S. A., Gunn, J. E., Uomoto, A., et al. 2013, *AJ*, 146, 32
- Sohn, J., Geller, M. J., Zahid, H. J., et al. 2016, *ASTROPHYS J SUPPL S*, 20
- Spolaor, M., Kobayashi, C., Forbes, D. A., Couch, W. J., & Hau, G. K. T. 2010, *MNRAS*, 408, 272
- Toledo, I., Melnick, J., Selman, F., et al. 2011, *MNRAS*, 414, 602
- Trujillo, I., Feulner, G., Goranova, Y., et al. 2006, *Monthly Notices of the Royal Astronomical Society*, 373, L36
- van der Wel, A., Rix, H.-W., Wuyts, S., et al. 2011, *ApJ*, 730, 38
- van der Wel, A., Franx, M., van Dokkum, P. G., et al. 2014, *ApJ*, 788, 28
- van Dokkum, P. G., Abraham, R., & Merritt, A. 2014, *ApJL*, 782, L24
- van Dokkum, P. G., Whitaker, K. E., Brammer, G., et al. 2010, *ApJ*, 709, 1018
- Veale, M., Ma, C.-P., Greene, J. E., et al. 2018, *Monthly Notices of the Royal Astronomical Society*, 473, 5446
- Villaume, A., Conroy, C., Johnson, B., et al. 2017, *ASTROPHYS J SUPPL S*, 230, 23
- Vogelsberger, M., Genel, S., Springel, V., et al. 2014, *MNRAS*, 444, 1518
- Wake, D. A., Bundy, K., Diamond-Stanic, A. M., et al. 2017, *The Astronomical Journal*, 154, 86
- White, S. D. M., & Rees, M. J. 1978, *Monthly Notices of the Royal Astronomical Society*, 183, 341
- Williams, B. F., Ciardullo, R., Durrell, P. R., et al. 2007, *ApJ*, 656, 756
- Yan, R., Bundy, K., Law, D. R., et al. 2016, *The Astronomical Journal*, 152, 197
- Yan, R., Tremonti, C., Bershady, M. A., et al. 2016, *AJ*, 151, 8
- Zahid, H. J., Kudritzki, R.-P., Conroy, C., Andrews, B., & Ho, I.-T. 2017, *ApJ*, 847, 18
- Zibetti, S., White, S. D. M., Schneider, D. P., & Brinkmann, J. 2005, *MNRAS*, 358, 949
- Zwicky, F. 1951, *Publications of the Astronomical Society of the Pacific*, 63, 61

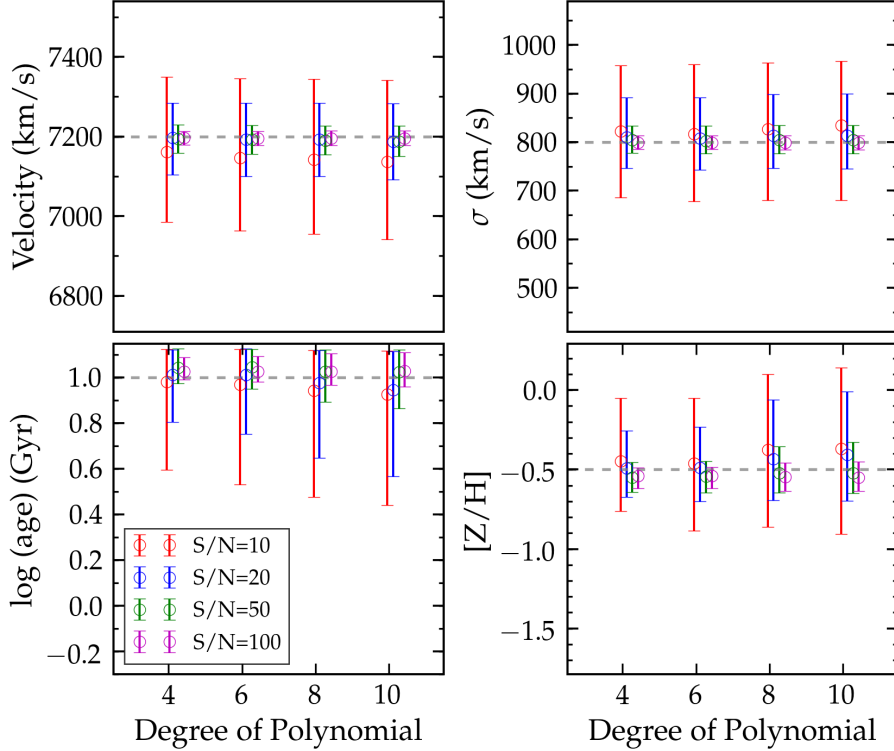


**Figure 12.** Test of recovery of recession velocity, velocity dispersion, age and overall metallicity  $[Z/H]$  with high velocity dispersion mock spectra by tuning the order of polynomial used to fit the continuum. The default degree of polynomial is  $(\lambda_{max}-\lambda_{min})/100\text{\AA}$ . We constructed 10 realizations at each S/N. The figure shows the mean values of these 10 realizations. Red, blue, green and purple symbols show parameters at 50 th percentile with spectra at S/N of 10, 20, 50 and  $100\text{\AA}^{-1}$ , respectively. Error bars enclose 16 th to 84 th percentiles. Gray dashed lines indicate the input values. For ICL spectra we use a 6 th order polynomial.

## APPENDIX

In this Appendix we examine our ability to recover the recession velocity, velocity dispersion, age and overall metallicity for ICL-like spectra with `alf`. The ICL presents a few related unique challenges due to the low S/N and very high velocity dispersions.

We begin by exploring the effect of the continuum normalization on the derived parameters. Our default approach is to set the degree of polynomial as  $(\lambda_{max}-\lambda_{min})/100\text{\AA}$ , which means a 10th order polynomial in the wavelength range  $3800 - 5700\text{\AA}$ . We test the sensitivity of the results to the polynomial degree in Figure 12. We have constructed a mock spectra dataset with ten realizations at a range of S/N from 10 to  $100\text{\AA}^{-1}$ . We assumed the mock spectra have a true recession velocity of  $7200 \text{ km s}^{-1}$ , a velocity dispersion of  $800 \text{ km s}^{-1}$ , an age of 10 Gyr and a metallicity of  $[Z/H] = -0.5$ . The data are fit over two wavelength ranges,  $4000-4700\text{\AA}$  and  $4700-5700\text{\AA}$ . The results are shown in Figure 12 as a function of the highest degree of the polynomial used in fitting the continuum. To test the appropriate order of polynomial term to use, we fit mock spectra with different assumption of this order from three to ten. It turns out this degree is crucial to our results. The velocity dispersion and low metallicity make it difficult to extract absorption features. If a high order polynomial is used to fit the continuum, real absorption features could be misinterpreted as part of the continuum, thus producing a biased result. As shown in Figure 12, a high order polynomial slightly biases age and metallicity, especially for low S/N spectra, and results in larger errorbars. The figure shows that the recession velocity and velocity dispersion can be recovered at good precision for mock spectra at all S/N. The biased recession velocity from the true value is within  $50 \text{ km s}^{-1}$ , and the biased velocity dispersion are no more than  $20 \text{ km s}^{-1}$  different if we adopt a highest degree of polynomial smaller than 6. Even for  $S/N \leq 20$  mock spectra, age and  $[Z/H]$  can be recovered well if we choose the right degree of polynomial to fit the continuum. In

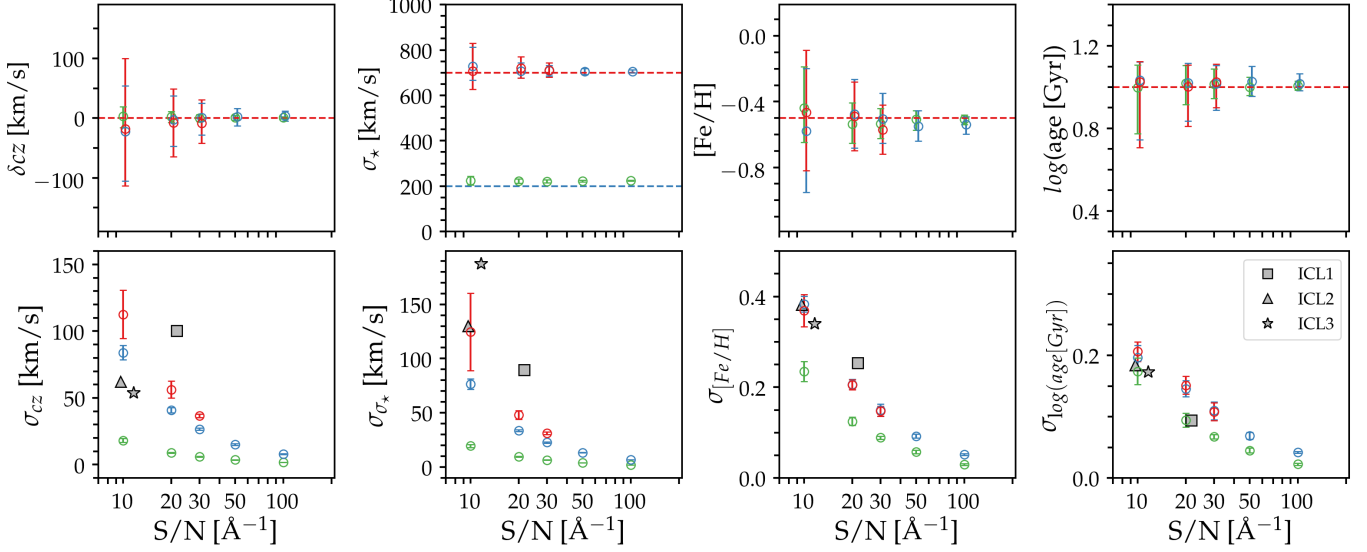


**Figure 13.** Recovery of parameters using mock spectra of systems with low ( $200\text{km s}^{-1}$ , green) and high ( $700\text{km s}^{-1}$ , red and blue) velocity dispersion as a function of S/N. We constructed 10 realizations at each S/N. Top panels: recovered velocity, velocity dispersion,  $[\text{Fe}/\text{H}]$ , and stellar age, compared to the input values (dashed lines). Error bars enclose 16 th to 84 th percentiles; Bottom Panels: typical uncertainty on the recovered parameters. For stellar populations with high velocity dispersion ( $700\text{km s}^{-1}$ ), their recovered parameters have larger errorbars. The uncertainty of stellar population parameters from fitting the ICL spectra are compared (gray).

this paper, we choose to use a polynomial with the highest degree of 6 to fit the ICL spectra. The mean bias on age is 0.6 and 0.3 Gyr at  $S/N=10\text{\AA}^{-1}$  and  $S/N=20\text{\AA}^{-1}$ , and the mean bias on  $[Z/\text{H}]$  is 0.04 and 0.01 dex, respectively.

The stellar absorption features in the ICL spectra are much weaker compared to typical ETG spectra due to the higher velocity dispersion of the former (Figure 5). As a consequence, the uncertainties on derived parameters are likely to be higher for the ICL than for ETGs, at a given S/N. We explore this issue in Figure 13, where we show recovered parameters, and uncertainties, as a function of S/N for an ETG-like dispersion ( $200\text{km s}^{-1}$ ) and an ICL-like dispersion ( $700\text{km s}^{-1}$ ). We also include in the lower panels the actual uncertainties and S/N values for the three ICL regions in the Coma cluster. At S/N of  $10 - 20\text{\AA}^{-1}$ , which is similar to the S/N we achieved in the spatially stacked ICL spectra, the uncertainty in  $[\text{Fe}/\text{H}]$  is about 0.1 dex larger than that derived from fitting typical ETG spectra. We also construct mock spectra with high ( $700\text{ km s}^{-1}$ ) velocity dispersion, but the S/N in  $3800\text{\AA}$  to  $4000\text{\AA}$  is only 60% of that in the rest part of spectra (red), similar to the non-uniform S/N in the ICL data. Although the uncertainties on  $[\text{Fe}/\text{H}]$  and stellar age are similar to the case of uniform S/N, the error constraints on recession velocity and velocity dispersion are worse. The results of three ICL regions are shown as a comparison. Their error constraints are closer to what we found in the mock data with high velocity dispersion and nonuniform spectra uncertainty.